Title

Four-dimensional quantitative analysis of cell plate development in Arabidopsis using lattice light sheet microscopy identifies robust transition points between growth phases.

Journal

Journal of Experimental Botany, 75(10)

Authors

Sinclair, Rosalie

Wang, Minmin

Jawaid, Muhammad

et al.

Publication Date

2024-05-20

DOI

10.1093/jxb/erae091

Peer reviewed

Journal of Experimental Botany, Vol. 75, No. 10 pp. 2829–2847, 2024
https://doi.org/10.1093/jxb/erae091 Advance Access Publication 4 March 2024

RESEARCH PAPER

Four-dimensional quantitative analysis of cell plate development in Arabidopsis using lattice light sheet microscopy identifies robust transition points between growth phases

Rosalie Sinclair[1], Minmin Wang[1], Muhammad Zaki Jawaid[2], Toshisangba Longkumer[1], Jesse Aaron[3], Blair Rossetti[3], Eric Wait[3,†], Kent McDonald[4], Daniel Cox[2], John Heddleston[3], Thomas Wilkop[5], and Georgia Drakakaki[1,*]

[1] Department of Plant Sciences, University of California Davis, Davis, CA, USA
[2] Department of Physics and Astronomy, University of California Davis, Davis, CA, USA
[3] Janelia Research Campus, Ashburn, VA, USA
[4] Electron Microscope Laboratory, University of California, Berkeley, CA, USA
[5] Department of Molecular and Cellular Biology, Light Microscopy Imaging Facility, University of California Davis, Davis, CA, USA
[†] Present address: Elephas Biosciences, Madison, WI, USA

* Correspondence: gdrakakaki@ucdavis.edu

Received 20 September 2023; Editorial decision 12 February 2024; Accepted 29 February 2024

Editor: Anja Geitmann, McGill University, Canada

Abstract

Cell plate formation during cytokinesis entails multiple stages occurring concurrently and requiring orchestrated vesicle delivery, membrane remodelling, and timely deposition of polysaccharides, such as callose. Understanding such a dynamic process requires dissection in time and space; this has been a major hurdle in studying cytokinesis. Using lattice light sheet microscopy (LLSM), we studied cell plate development in four dimensions, through the behavior of yellow fluorescent protein (YFP)-tagged cytokinesis-specific GTPase RABA2a vesicles. We monitored the entire duration of cell plate development, from its first emergence, with the aid of YFP–RABA2a, in both the presence and absence of cytokinetic callose. By developing a robust cytokinetic vesicle volume analysis pipeline, we identified distinct behavioral patterns, allowing the identification of three easily trackable cell plate developmental phases. Notably, the phase transition between phase I and phase II is striking, indicating a switch from membrane accumulation to the recycling of excess membrane material. We interrogated the role of callose using pharmacological inhibition with LLSM and electron microscopy. Loss of callose inhibited the phase transitions, establishing the critical role and timing of the polysaccharide deposition in cell plate expansion and maturation. This study exemplifies the power of combining LLSM with quantitative analysis to decode and untangle such a complex process.

Abbreviations: AIC, Advanced Imaging Center; CSL, cellulose synthase-like protein; ES7, Endosidin 7; LLSM, lattice light sheet microscopy; MS, Murashige and Skoog; PFS, planar fenestrated sheet; ROI, region of interest; TN, tubular network; TVN, tubular–vesicular network YFP, yellow fluorescent protein.

Keywords: Callose, cell plate, cytokinesis, 4D imaging, lattice light sheet microscopy, plant cell division, quantitative image analysis, RABA2a.

Introduction

Cytokinesis is a fundamental process in life, determining growth, development, and differentiation. In plant cytokinesis, a process fundamentally different from cytokinesis in animals and fungi (Samuels *et al.*, 1995; Staehelin and Hepler, 1996; Jürgens, 2005; Drakakaki, 2015; Gu and Rasmussen, 2022; Sinclair *et al.*, 2022), *de novo* formation of a cell plate partitions the cytoplasm of the dividing cell. Cell plate development occurs in multiple stages. It requires the directed and choreographed accumulation of post-Golgi vesicles via the phragmoplast (a structure composed of cytoskeletal polymers, associated proteins, and membranes) at the division plane (Lee and Liu, 2013; Smertenko, 2018).

Cell plate expansion is centrifugal, led by the accumulation and fusion of vesicles arriving at the leading edge.Various morphologically determined cell plate developmental stages exist simultaneously during cytokinesis (Samuels *et al.*, 1995; Seguí-Simarro *et al.*, 2004). First, during the fusion of vesicle stage (FVS), cytokinetic vesicles guided by the phragmoplast arrive at the division plane where fusion occurs. Upon vesicle fusion and fission, membrane tubulation, primarily due to the activity of dynamin-related proteins (Otegui *et al.*, 2001; Seguí-Simarro *et al.*, 2004), helps the transition to a tubular–vesicular network (TVN) (Samuels *et al.*, 1995; Seguí-Simarro *et al.*, 2004). The membrane morphology evolves through the expansion of the network to a smoother tubular network (TN). The polysaccharide callose is predominantly deposited at this stage (Samuels *et al.*, 1995). The excess membrane material is recycled via clathrin-coated vehicles (Otegui *et al.*, 2001). As the cell plate smoothens and expands, it transitions to a planar fenestrated sheet (PFS). The cell plate stiffens with the deposition of polysaccharides, leading to the formation of a cross-wall. As the phragmoplast expands centrifugally, delivering vesicles to the leading edge of the cell plate, the center matures with the removal of excess membranes and deposition of polysaccharides. Thus, at any given time, the cell plate contains a gradient of developmental stages. A recent review (Sinclair *et al.*, 2022) includes an animated overview of cytokinesis.

The synchronous and timed deposition of membrane material and polysaccharides control the cell plate's expansion, stability, and maturation into a new cross-wall (Drakakaki, 2015; Smertenko *et al.*, 2017; Gu and Rasmussen, 2022). However, little is known about how these mechanisms are orchestrated (Drakakaki, 2015; Smertenko *et al.*, 2017). Many GTPases are localized at the cell plate (Chow *et al.*, 2008; Geldner *et al.*, 2009; Qi *et al.*, 2011; Qi and Zheng, 2013; Berson *et al.*, 2014; Mayers *et al.*, 2017; Shi *et al.*, 2023), including the Rab-related GTPase RABA2a, which is involved in the delivery of *trans*-Golgi network-derived vesicles to the leading edge of the cell plate. As such, RABA2a is considered a good marker for cytokinetic vesicle accumulation directing cargo to the cell plate (Chow *et al.*, 2008). Necessary, vesicular fusion events during Arabidopsis cell plate formation are mediated by SNARE complexes that involve KNOLLE and its partners (El Kasmi *et al.*, 2013).

Our current insights into cell plate formation are based on two-dimensional, electron (Samuels *et al.*, 1995; Seguí-Simarro *et al.*, 2004) and *in vivo* fluorescence micrographs, with only minimal contributions from multidimensional spatiotemporal data (reviewed in Drakakaki, 2015; Smertenko *et al.*, 2017; Sinclair *et al.*, 2022; Geitmann, 2023). During the TN stage, callose, a β-1,3-glucan polysaccharide, is temporally integrated into the cell plate (Samuels *et al.*, 1995). It is proposed that callose contributes a spreading force in the stabilization and maturation of the cell plate (Jawaid *et al.*, 2022). However, its timely delivery and contribution to the stage progression of cytokinesis remain elusive. Dissecting the dynamic behavior of components such as callose and other polysaccharides, and the overall phragmoplast machinery, is essential for a comprehensive understanding of their contributions. Even with the advancement in many technologies, research into cell plate development is hindered by the fact that mutations in cytokinesis, such as those of callose synthase/glucan synthase like (GSL8), are often lethal (Desprez *et al.*, 2007; Chen *et al.*, 2009; Thiele *et al.*, 2009), making a genetic approach to the underlying questions unfeasible. Therefore, imaging modalities that allow observation of the whole cytokinesis process in space and over time, with high image quality, are required to improve our understanding.

So far, confocal-based modalities are not ideal as they exhibit significant photobleaching, making it very challenging to capture with high temporal resolution the entire process of cell plate formation from initiation to maturation. In order to identify a region in the seedling where cell plates will develop requires a dedicated marker that labels the phragmoplast, such as TUA6 (Ueda *et al.*, 2003), and/or a nuclear stain suitable for live cell imaging. For a cytokinetic vesicle marker, such as RABA2a, the presence of an already initiated cell plate is required to set up the image acquisition, which in turn compromises early-stage observations. Additional challenges include: balancing field of view with temporal resolutions and inherent growth motion of the seedling laterally and axially. In the absence of automated tracking algorithms, manual adjustments in x, y, and z are often required. These go hand in hand with extensive post-data processing, including concatenation and alignment.

Recent technological and methodological advances are now allowing four-dimensional (4D, *XYZT*), *in vivo* fluorescence microscopy, which can provide more biologically relevant quantitative information. The development of lattice light sheet microscopy (LLSM) enables lengthy image acquisitions with significantly minimized photobleaching. LLSM is a promising avenue in dissecting mitosis across different biological systems. It is allowing for easier acquisition of multiple cytokinesis events simultaneously, from their earliest detection, while decreasing the constant need to manually track the cell plate during acquisition (Chen *et al.*, 2014; Aguet *et al.*, 2016). In plants, LLSM has been employed to reveal the spatiotemporal accumulation of Annexin 1 – green fluorescent protein (ANN1-GFP) around the nuclear envelope of elongating trichoblasts (Tichá *et al.*, 2020), the dynamic subcellular localization of ROOT HAIR DEFECTIVE 2 (GFP–RHD2), as well as the observation of fine actin filaments in young root hairs (Ovecka *et al.*, 2022). However, while LLSM is an enabling modality, it has not yet been adopted to study cytokinesis in plants, potentially in part due to the efforts required to establish an imagining and quantitative analysis routine.

In this study, we adopted LLSM to study cytokinesis in plants. Taking advantage of the unique capabilities of LLSM, we investigated cell plate dynamics using the cytokinesis marker yellow fluorescent protein (YFP)–RABA2a coupled with pharmacological inhibition of callose. Quantitative analysis revealed the presence of distinct phases, with easily identifiable transition points during cell plate development, which were altered by inhibition of callose. The here presented imaging pipeline together with the identified stage transition can help further unravel the complex process of cytokinesis and interrogate the biological role of its components.

Materials and methods

Plant materials and growth

All Arabidopsis (*Arabidopsis thaliana*) seedlings were grown as described previously (Park *et al.*, 2014). Briefly, seeds were sterilized for 10 min in a solution containing 10% (v/v) sodium hypochlorite (NaOCl)/80% (v/v) ethanol/10% (v/v) water, followed by three washes in 90% (v/v) ethanol for 1 min, and subsequently air dried. Seeds were germinated on square plates containing Murashige and Skoog (MS) medium (Sigma; one-quarter strength), supplemented with 1% (w/v) Suc, pH 5.7, solidified with 0.5% (w/v) phytagel (Sigma) and designated chemicals. Plates were incubated at 10° off the vertical in a growth room with a 16 h light/8 h dark photoperiod for 3–5 d. Transgenic lines expressing YFP–RABA2a (Chow *et al.*, 2008) were used to observe cell plate development with or without chemical treatment (Park *et al.*, 2014).

Chemical treatment and staining procedures

For microscopy, seedlings were grown as described above for 3 d and then transferred to 48-well plates containing 2 ml of liquid MS medium supplemented with 390 mM DMSO (Sigma), 50 μM Endosidin 7 (ES7) (ChemBridge) (or otherwise indicated concentration) and allowed to grow for 2 h as pulse treatment. Chemicals were diluted to their working concentrations from 1000× stock solutions. FM4-64 (5 μM) diluted 1:1000 from a stock solution, applied for 5 min, was used to stain the plasma membrane. Aniline blue fluorochrome (Biosupplies) was used to detect callose at 0.1 mg ml^{-1} in water, diluted from 1 mg ml^{-1} stock. Staining was performed directly on imaging slides.

Transmission electron microscopy

Four-day-old Arabidopsis seedlings, treated with 50 μM ES7 for 1 h, were analyzed by transmission electron microscopy (TEM). Root tips (1 mm) were excised and fixed using high-pressure freezing methods as described earlier (McDonald, 2014; Otegui, 2020). Excised root tips were placed in a type B freezing planchette containing yeast paste as a filler/cryoprotectant and frozen under high pressure in a high-pressure freezing unit (BAL-TEC HPM 010). Freeze substitution was performed in 1% OsO_4 and 0.1% uranyl acetate in acetone, followed by infiltration and embedding in Epon resin as described earlier (McDonald and Webb, 2011; McDonald, 2014). Thin sections (70 nm) were cut on a Leica Ultracut E ultramicrotome, picked up on Formvar-coated slot or 100 mesh grids, and post-stained for 7 min in 2% uranyl acetate in 70% methanol, followed by 4 min staining in Reynold's lead citrate. Images were taken with a Gatan Ultrascan 1000 camera on a FEI Tecnai-12 electron microscope operating at 120 kV.

Confocal/high resolution microscopy

Image aquisition

A Zeiss Airyscan 980 or a Leica SP8 was used for confocal imaging. The Leica SP8 was used to image YFP–RABA2a seedlings co-stained with FM4-64 (5 μM) utilizing a ×100/1.4 NA oil objective (HC PL APO CS2) employing a high resonant scanning with line averaging set to 15. Excitation at 512 nm was used for both YFP–RABA2a and FM4-64, with emissions collected at 520–558 nm and 650–800 nm for YFP and FM4-64, respectively. For the time-lapse series, *Z*-stacks were collected at intervals of ~1 min for 30–45 min. Images are representatives of five biological replicates (independent seedlings).

The Zeiss 980 was used to image YFP–RABA2a seedlings co-stained with aniline blue at single time points, using Airyscan CO 8Y mode. The fluorescent signal of YFP–RABA2a was exited using a 514 nm laser at 25% power, and aniline blue fluorochrome was excited using the 405 nm laser at 15% power. All images were collected using the LD LCI Plan-Apochromat ×40/1.2 NA (Korr DIC M27) water objective. Images are representatives of five biological replicates (independent seedlings).

The Zeiss 980 was used to image Arabidopsis seedlings treated for 2 h with 50 μM ES7 or DMSO and co-stained with 5 μM FM4-64. The fluorescent signal of FM4-64 was excited using a 514 nm laser at 10% power. All images were collected using the LD LCI Plan-Apochromat ×40/1.2 NA (Korr DIC M27) water objective. Images are representatives of 20 biological replicates (independent seedlings).

Image processing

Leica SP8 data were deconvolved using classic maximum likelihood estimation (CMLE), manually adjusting for background with a maximum of 20 iterations and corrected for *XYZ* drift using Huygens (SVI). Collected images from the Zeiss 980 Airyscan were processed using the Zeiss built-in Airyscan processing software employing automated settings. All data were exported to Imaris (Oxford Instruments) for segmentation and 3D or 4D visualization. Figures were assembled using Affinity Designer (Serif).

Lattice light sheet microscopy

Imaging

Imaging was performed using the lattice light sheet microscope at the Advanced Imaging Center (AIC) on the Janelia Research Campus,

following sample preparation and imaging procedures as previously described (Chen *et al*., 2014). Arabidopsis seedlings at 3–4 d old were mounted on a 5 mm coverslip [Warner Instruments Cat. No 64-0700 (CS-5R)]. One seedling was mounted per coverslip within a thin layer of 0.5% low melting agarose (w/v) in water. The cover slip was clipped to the end of a long extension of the sample holder and submerged in a bath filled with 8.5 ml of 1/4-strength MS liquid medium. The opposite end of the coverslip holder was bolted to the sample piezo (Chen *et al*., 2014). YFP–RABA2a plants were stained with FM4-64, and both fluorophores were excited using a 488 MPB fiber laser. A two-camera system, 2× Hamamatsu Orca Flash 4.0 v2 sCMOS, was used to acquire the images of the two fluorophores.

Lattice light sheet microscopy image processing

All data were acquired in the dithered mode and were deconvolved by using a Richardson–Lucy algorithm adapted to run on a graphics processing unit (GPU) (NVIDIA, GeForce GTX TITAN), using an experimentally measured point spread function (PSF) for each emission wavelength. Before visualization, all 3D datasets acquired via sample scan in the x, y, and z coordinated system were transformed ('deskewed') to the more conventional x, y, and z coordinates using a GPU.

Selection of points of interest for channel alignment and image stabilization

Channel alignment

The BigStitcher plugin in ImageJ was used to process datasets before quantitative analysis. All files using BigStitcher were converted to .xml to register how the data are stored and track any internal processing following the pipeline described in the AIC guidelines: https://knowledge.aicjanelia.org/posts/20200730-stabilize-roi-selection/. One .xml file was generated per time-lapse dataset. For our experiments, the metadata denoted FM4-64 as channel 0 and YFP–RABA2a as channel 1.

Once a file was generated, channel alignment was applied first, followed by drift correction (movement in the field of view). Note that the drift correction can lead to misalignment if processing is conducted in this sequence. Channel alignment followed a similar routine to the drift correction, as described in AIC guidelines: https://knowledge.aicjanelia.org/posts/20200730-stabilize-roi-selection/ with the following modifications.

(i) In the Multiview Explorer window, the first time point was selected for channel 0 (FM4-64), and the command 'Detect Interest Points' was used for navigation to the interest points 'Difference-of-Gaussian' with no other restrictions selected. This was repeated for channel 1 (YFP–RABA2a).

(ii) Then the parameters used to identify the points of interest were refined using the sigma and threshold sliders. The minimum threshold was used to detect the space within each cell, enabling the individual selections of interest for each cell. Sigma values were set to a range of 8–9 to obtain detectable points/regions inside each cell that can be used for the alignment. Adjustments were made to create the best recognizable points common between the two channels to facilitate the best alignment in the next step.

(iii) The points of interest were registered using a precise descriptor-based (translation-invariant) algorithm to align the two channels and validate them through the viewer window 3D function. The transformation model is rigid, with an allowed error for random sample consensus iterative methodology known as RANSAC (px) of 7–8. This was repeated for various sigma thresholds until the two channels overlapped.

(iv) Once complete, the BigStitcher windows were closed, and in the plugins menu the following sequence was selected: Multiview Reconstruction→Batch Processing→Tools→Duplicate Transformations. Transform one-time points to other time points. The selected transformation was then applied to all time points across the dataset.

Drift correction

Following channel alignment, drift correction was applied using the steps below as described in the AIC guidelines: https://knowledge.aicjanelia.org/posts/20200730-stabilize-roi-selection/. Note the significant differences from the channel alignment steps: (i) the use of all time points in one channel, instead of the first time point and (ii) the adjustment of Gaussian values to identify the cell wall corners across the time points, instead of the space inside the cells that was used for channel alignment. The threshold was set to the maximum, while the sigma value was set to a range from 7.5 to 9.5.

Create a bounding box for the region of interest

Region of interest (ROI) selection and export as 3D .tiffs were used to decrease file size and obtain workable files by following the steps 'Create Bounding Box for Region of Interest' as outlined in AIC guidelines: https://knowledge.aicjanelia.org/posts/20200730-stabilize-roi-selection/.

Image stack assembly and bleach correction

The .tiff files generated from the bounding box ROI step were then separated into folders by each channel and concatenated into a full-time series using ImageJ. The time series were then bleach-corrected using histogram matching. Finally, processed data were first exported into individual .tiffs and subsequently into the .ims format using the Imaris file converter. Before converting, settings were adjusted for the voxel dimension, *XYZT* frame, and image acquisition time points. Files were finalized and imported into Imaris for 4D volumetric rendering. All time series at this step contained two datasets, one for 'raw' data and one for the histogram-matched bleach-corrected data.

Representative datasets used in the study are available on Zenodo at https://doi.org/10.5281/zenodo.10515765.

Imaris segmentation

Surface rendering of individual cell plates was performed with the surface creation tool using Imaris X64 9.6.0 in conjunction with object tracking as outlined by user guidelines, https://qbi.uq.edu.au/research/facilities/microscopy-facility/image-analysis-user-guides/analysis-software/imaris/creating-surface-imaris, with the following modifications. (i) In the first step of the surface creation, a bounding box was drawn to enable the separation of a specific region to reduce the working file size. (ii) Surface segmentation was performed using the 'new surfaces' function. The appropriate channel (histogram corrected) was used. Surface detail was set to 0.1 µm, and thresholding was based on background subtraction with the values set based on the diameter of the largest sphere fitting the object. To obtain these values, the diameter of the largest shape was measured in the 2D view under the slice mode. (iii) During the next step, the image histogram was adjusted to best fit the objects of interest. Multiple surfaces/segmentations could be used for different cell plates and different time points for statistical analysis. (iv) In the next step, a preview was generated by Imaris, with the final surfaces bounding all the objects that were detected in the ROI. Objects were filtered based on voxel count to better define the observed objects. In general, a voxel count of 20 throughout the dataset allowed for the best observation. Surfaces were tracked throughout the time course with autoregression motion selected, and the maximum travel distance between time points was set to 4 µm. The maximum gap size for surfaces in consecutive frames in a track was set to 3. (v) Following surface rendering, individual cell plates were segmented by selecting their corresponding subsurfaces, rebuilding the cell plate individual tracks, and connecting the subtracks together. Surfaces

and volumes of cell plates were extracted, uniquely named, and quantitatively analyzed.

We note that working with different channels separately leads to manageable file sizes matching better the computer processing power. As the different channels are aligned, they can be later combined after further processing. (vi) Cell plate diameter values were recorded manually for each time point during cell plate formation by measuring the largest distance of YFP–RABA2a. The FM4-64 plasma membrane stain was employed to determine the predicted cross-wall width and was used to normalize the diameters, accounting for cell size variations (Chow *et al.*, 2008; van Oostende-Triplet *et al.*, 2017). Finally, normalized diameter values were averaged at their respective time points across cell plates.

Quantification and statistical analysis

The data generated from the intensity-based Imaris segmentation were compiled in Excel files and further analyzed (Supplementary Tables S1, S2). The Origin 2021 software (Origin. 2003. Origin 7.5. OriginLab Corp., Northampton, MA, USA) was used to normalize the data to their maximum volume or area. To determine an approximate rate of change of measured volumes/areas, the data were fitted to a polynomial (adjusted R^2 0.69 ± 0.03), from which derivatives were calculated. For visualization purposes, the derivatives were linearly shifted, creating a time when all rates passed through zero. However, raw datasets were considered for fitness comparison and any further statistical analysis differences.

Binning approach for further statistical analysis

For statistical comparison of volume accumulation between control and ES7 treated samples, the data were divided into five groups (bins) for further statistical analysis. These bins correspond to the normalized volume changes based on the following approach: bin 1 (increasing values from 0 to 0.33 μm^3), bin 2 (increasing values from 0.33 μm^3 to 0.66 μm^3), bin 3 (increasing values from 0.66 μm^3 to 1 μm^3), bin 4 (decreasing values from 1 μm^3 to 0.66 μm^3), bin 5 (decreasing values from 0.66 μm^3 to 0.33 μm^3), and bin 6 (decreasing values from 0.33 μm^3 until reaching the final minimal YFP–RABA2a cell plate volume). The width of the bins, as well as the divide between increasing and decreasing values, were chosen for simplicity. The derived rates from each of the volume bins were then averaged. These averages were statistically analyzed using two-tailed pairwise *t*-tests (GraphPad) and then were plotted.

P-values for diameter studies were additionally calculated using a second binning approach. The normalized diameter values were averaged across cell plates at their respective time points. For comparisons, The ES7 time points were laterally adjusted such that the averaged ES7 values at the starting point matched the corresponding control value. *P*-values were then calculated using pairwise *t*-tests (GraphPad).

Results

Development of a 4D lattice light sheet microscopy image acquisition and processing pipeline to study plant cytokinesis

Cell plate assembly, expansion, and maturation are regulated in space and time over an extended period. Therefore, 4D imaging is necessary to examine in depth the membrane and cell plate expansion dynamics. We first used laser scanning confocal microscopy with a resonance scanner, maximizing acquisition speeds, to follow cytokinesis over extended periods of time. Using YFP–RABA2a (Chow *et al.*, 2008) as a cytokinesis marker, high resolution imaging of cell plate development was possible (Fig. 1). Time-lapse imaging showed centrifugal expansion of the cell plate. This approach, however, was not sustainable for the dissection of a large number of cytokinesis events. With confocal microscopy, one could only manually track developing cell plates, one at a time, limiting its scalability. Further, using this approach, only already sufficiently assembled cell plates could be imaged since their presence was necessary to set up the acquisition.

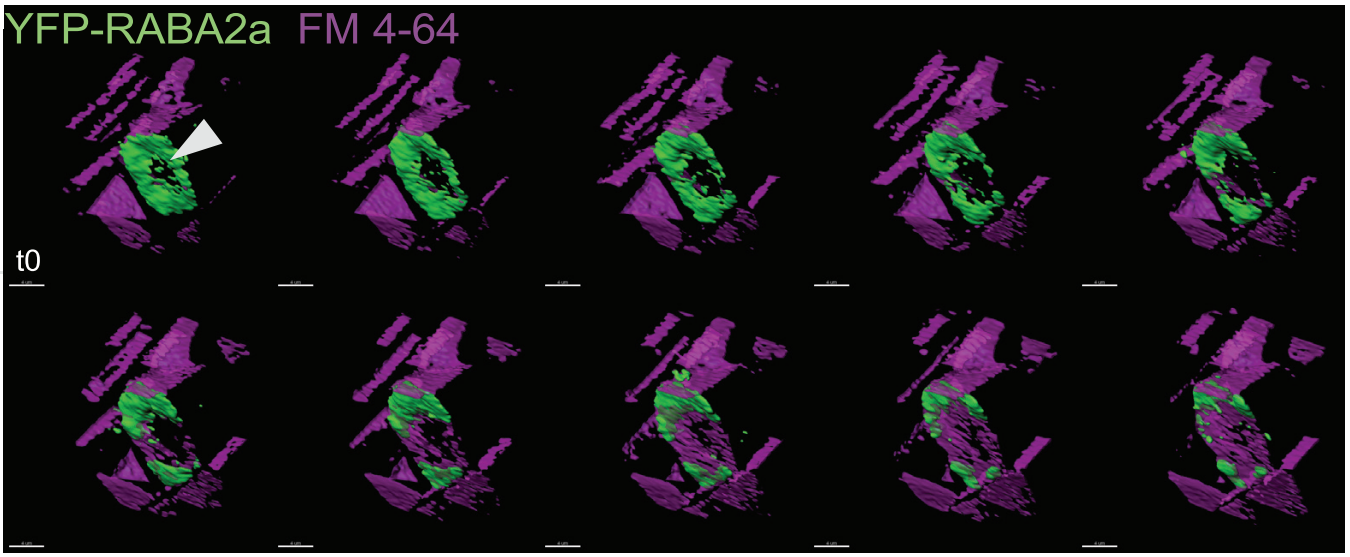

Fig. 1. YFP–RABA2a dynamics at the cell plate. YFP–RABA2a (green) vesicle accumulation and FM4-64- (purple) stained plasma membrane show the transition from vesicle accumulation to mature membrane throughout cell plate development in untreated plants. The accumulation of YFP–RABA2a at the cell plate periphery during maturation with a concurrent increase in the membrane content in the center shows centrifugal growth and maturation. The arrow indicates RABA2a at the cell plate. Data were collected on a Leica SP8 microscope. Scale bar=4 μm. Δ*t*=1 min.

To circumvent these hurdles and capture full cell plate events, while improving throughput, we used LLSM. LLSM affords imaging at much faster rates and with less light exposure of the sample, minimizing photobleaching and phototoxicity (Chen *et al*., 2014). LLSM helps to extend the observation time, while affording higher axial resolution with similar lateral resolutions to those obtained with confocal microscopy. Using LLSM, we recorded the marker YFP–RABA2a in the root tips of 3-day-old *A. thaliana* seedlings. We generated 4D data capturing the complete process of cell plate development with minimal photobleaching, allowing the acquisition of datasets amenable to in-depth quantitative analysis. The cell membrane and cellular architecture dye, FM4-64, was used to provide a reference for overall cell shape and cell plate expansion perspective. Once image acquisition was completed, a pipeline was developed primarily using open-source software for image processing followed by quantitative analysis (Fig. 2, see more details in the Materials and methods). In brief, this involved image deskewing, aligning the two fluorescence channels, correcting for (*XYZ*) drift, and selection of an ROI to obtain a manageable data size. Once data were exported into readable formats (.tiff), they were concatenated into time series stacks for each channel. The image files were bleach-corrected by histogram matching across time points for the whole stack (Fig. 2B, C). Segmentation of developing cell plates was performed using an intensity value-based algorithm in Imaris, followed by quantitative analysis of cell plate volume, surface area, and diameter (Fig. 2D).

Quantification of cell plate dynamics shows three distinct developmental stages based on YFP–RABA2a accumulation patterns

With the adoption of LLSM, cell plate growth from its point of origin at the vesicle accumulation stage (FVS) until completion of cytokinesis can be observed, a time frame that was not previously established with confocal and electron microscopy (Seguí-Simarro *et al*., 2004; Higaki *et al*., 2008; van

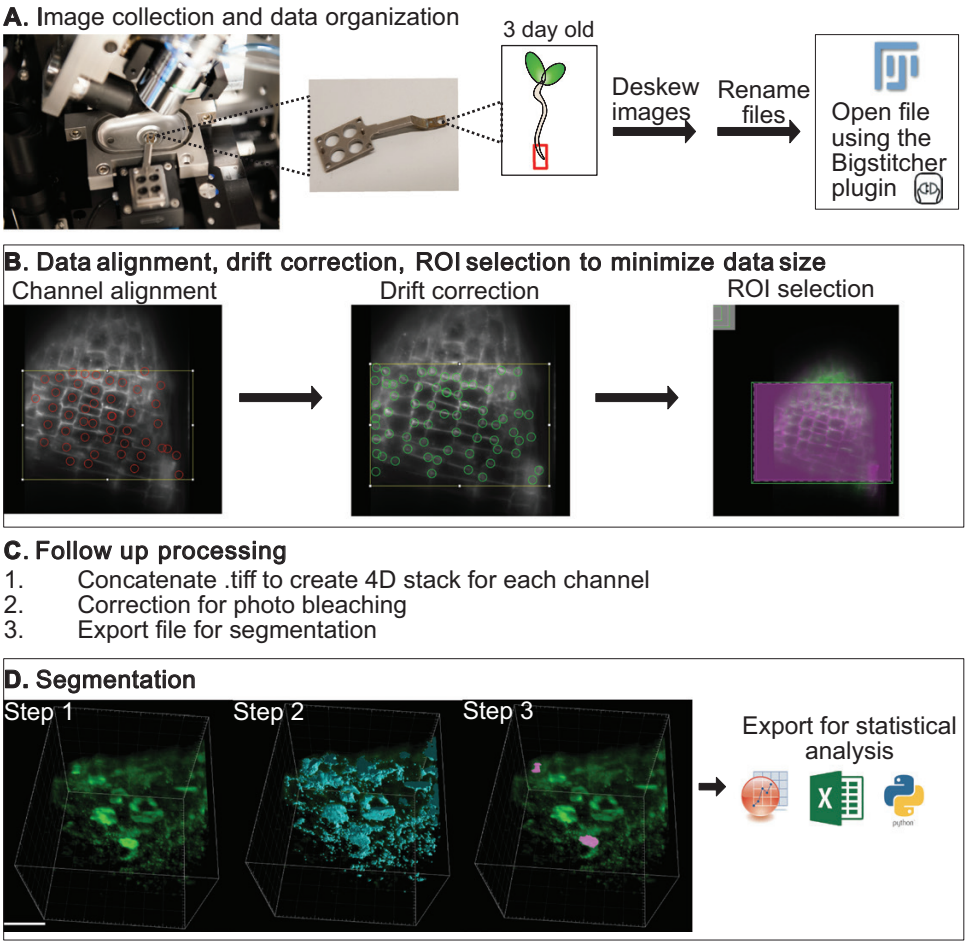

Fig. 2. Schematic representation of the lattice light sheet data processing pipeline. Schematic representation of the processing workflow for collecting plant cytokinesis events under lattice light sheet microscopy (LLSM). The workflow is separated into four overarching steps: (A) image collection and data organization; (B) data alignment with drift correction and ROI selection; (C) concatenation of each time point to create a 4D stack and bleach correction follow-up processing; (D) image segmentation and quantification. Scale bar=20 μm.

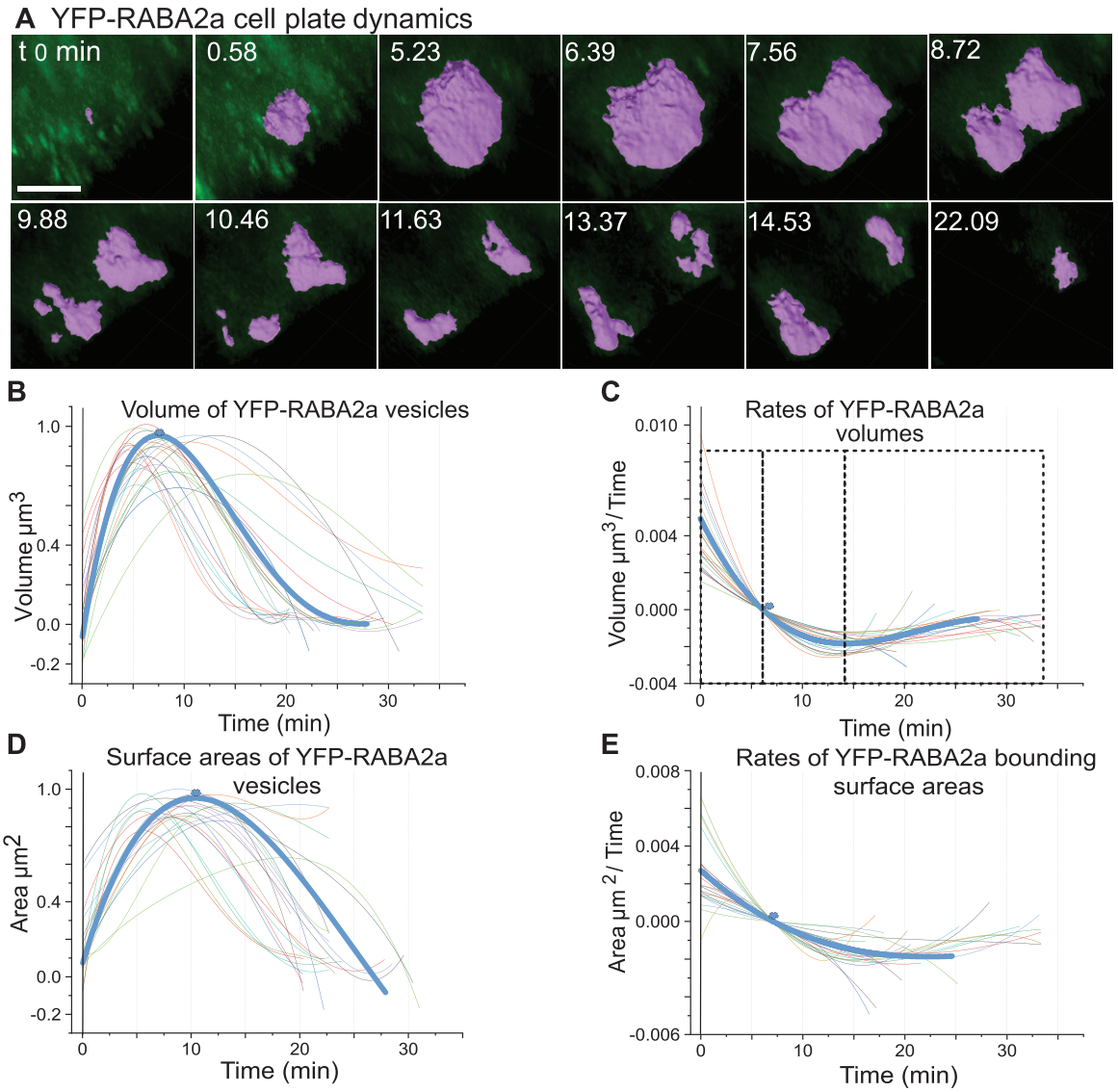

Fig. 3. Quantitative YFP–RABA2a dynamics at the cell plate. (A) Representative snapshots of a time series showing the transition of YFP–RABA2a (green) in segmented cell plates (purple) during their expansion and maturation. Scale bar=5 µm. (B and C) Volumes of segmented cell plates and their growth rates. (D and E) Bounding surface areas of segmented cell plates and their rates of change. Each line indicates an individually segmented cell plate. Note the cell plate shown in (A) is highlighted in bold in all graphs. Normalized volumes and bounding surfaces , respectively, of developing cell plates were fitted to a polynomial (B and D). Additionally, the polynomials (B and D) were used to derive the rates of change of the volume and bounding surface area (C and E). *n*=24.

Oostende-Triplet *et al.*, 2017; Geitmann, 2023). An example is presented in Fig. 3A, a pink segmented surface, in which volume and area change and rates are tracked by a bold blue line in Fig. 3B–E. As shown in Fig. 3A, B, completion of cytokinesis takes place within 20–30 min. Within this time window, cell plate volume peaked during the first 8 min (Fig. 3A). Then the cell plate expanded laterally and flattened, with the gradual reduction of the vesicle accumulation marker dispersing at the cell plate rim and finally disappearing (Supplementary Video S1), probably representing transitions to discontinuous phragmoplast stages (Smertenko *et al.*, 2017; Sinclair *et al.*, 2022). With LLSM, observation of multiple cytokinetic events within the same root tip was possible. Each observed cytokinetic event was unique. Events in the same root tip did not exhibit overreaching similarity.

A quantitative analysis of segmented cell plates based on the cytokinetic marker was performed to better understand the spatiotemporal dynamics of vesicle accumulation and cell plate expansion. Normalized volumes of developing cell plates were fitted to a polynomial regression, allowing accumulation trends to be observed across biological samples (Fig. 3B). As mentioned above, the cell plate volume accumulation based on YFP–RABA2a peaked within ~8 min, followed by a rapid reduction over the following 8 min. The rates of volume

(1.5×10^3–9.5×10^3 μm^3 min^{-1}) accumulation determined by the first-order derivative showed a net positive addition of YFP–RABA2a vesicle/membrane material for the first 8 min (Fig. 3C). Within this period, a short interval exhibits linear growth. The first 8 min marked a turning point at which the rates of volume accumulation switched to a net negative value (Fig. 3C, asterisk). The negative rate values probably represent recycling of large amounts of material during cell plate expansion and maturation, as postulated from electron microscopy analysis (Otegui *et al*., 2001; Seguí-Simarro *et al*., 2004). We also quantified the bounding surface area corresponding to the segmented cell plates. The time course of the YFP–RABA2a bounding surface areas and their corresponding rates (Fig. 3D, E) showed an overall similar trend in line with the volume accumulation. Without overinterpretation of the data, one can note that peak values are slightly deviating, which might be indicative for geometrical changes—thinning or thickening.

In summary, three distinct phases became apparent based on our quantification: phase I, a rapid phase of cytokinetic vesicle material delivery with a positive YFP–RABA2a cell plate volume rate, followed by a substantial volume reduction (phase II). Finally, a third phase (phase III) of minimal cytokinetic vesicle presence at the rim of the cell plate took place before joining the parental cell wall.

To correlate the dynamic behavior of YFP–RABA2a cytokinetic vesicles with that of the cell plate membrane, we quantitated both volumes and bounding surface areas. The membrane was visualized by staining with the endocytic lipophilic dye FM4-64. The segmentation of FM4-64-stained membranes throughout cytokinesis is not a trivial task, given that the staining is very much prone to indiscriminate staining of all membranes over time and/or bleaching. The inherently fluctuating time point for cell plate formation after the initiation of the staining is an additional challenge and limits available datasets. The temporal behavior of the YFP–RABA2a volumes and stained cell membranes for selected samples observed via LLSM (Supplementary Fig. S1A–D) and laser scanning confocal microscopy is shown in Supplementary Fig. S1; Supplementary Table S3.

The normalized and polynomial fitted data for both the YFP–RABA2a volume and membrane volume follow a similar pattern. Both exhibit a distinct and rapid growth phase of volume accumulation that, after reaching its zenith, is followed by a reduction at somewhat lower rates. The peaks for both YFP–RABA2a and the FM4-64 membrane occur at similar times. It is noteworthy, that the FM4-64 membrane removal dynamics exhibit higher dispersion, compared with the very coherent rates of the YFP–RABA2a volume. One can only speculate on the causative factors for this, with varying rates of membrane removal or incomplete FM4-64 staining (stain exhaustion) being possible reasons. Bounding surfaces follow similar trends for both YFP–RABA2a and FM4-64 staining (Supplementary Fig. S1C, D). Confocal data show a very similar pattern to that observed for the LLSM data. Both YFP–RABA2a volumes and FM4-64 membrane volumes follow similar dynamics, with distinct peaks at similar times (Supplementary Fig. S1E, F).

These data highlight the suitability of our global analysis of membrane volumes during cell plate development as a mechanism to decipher progression of cell plate formation consistent with earlier predictions based on electron microscopy (Otegui *et al*., 2001; Seguí-Simarro *et al*., 2004). In future studies, the use of the cytokinesis-specific SNARE KNOLLE (Lukowitz *et al*., 1996) might be a useful alternative for charting the membrane kinetics.

Inhibition of callose deposition arrests cytokinesis and induces aberrant membrane accumulation patterns

Our data show that while vesicle volume accumulation is a very rapid process, the expansion and maturation phase is lengthier. The latter stages are accompanied by a significant loss of cell plate volume, probably due to the recycling of membrane material. During the transition of the cell plate from a membrane network to a fenestrated sheet, the accumulation of the polysaccharide callose is implicated in stabilizing this network and providing a spreading force for expansion and maturation (Samuels *et al*., 1995; Jawaid *et al*., 2022). To better understand the role of callose during these dynamic cell plate transitions, we applied ES7, a small molecule that has shown inhibition of cytokinetic callose deposition and callose synthase activity in microsome assays (Drakakaki *et al*., 2011; Park *et al*., 2014). As observed by confocal microscopy, YFP–RABA2a accumulation was not affected by the 2 h ES7 pulse treatment. However, the cell plate expansion and maturation were impaired, leading to stagnation, as shown by the cytokinesis marker YFP–RABA2a and FM4-64 staining (Fig. 4). Quantification of cell plate stubs on seedlings stained with FM4-64 averaged three stubs per seedlings, while DMSO controls showed zero to rarely one cell plate stub (Supplementary Fig. S2A–C). We then used TEM on high-pressure-fixed root tips to resolve changes induced by ES7 at the ultrastructural level. Consistent with our confocal observations, no cell plate stubs were observed in DMSO controls (Supplementary Fig. S2D) while irregular cell plate structures were observed in ES7-treated roots (Supplementary Fig. S2E). As shown in Supplementary Fig. S2F, the structure of cytokinetic vesicles was not affected during the accumulation stage, and no discernible aberrations in the vesicle or Golgi morphology were observed. However, irregular cell plate stubs were observed in later stages of cytokinesis (Supplementary Fig. S2G, arrows) in contrast to normally expanding cell plates as previously reported in Arabidopsis (Samuels *et al*., 1995), corroborating our light microscopy observations.

Membrane transition between cytokinetic stages is affected by the chemical inhibition of callose

While informative, confocal and electron microscopy were not ideal for studying the dynamic nature of cell plate development

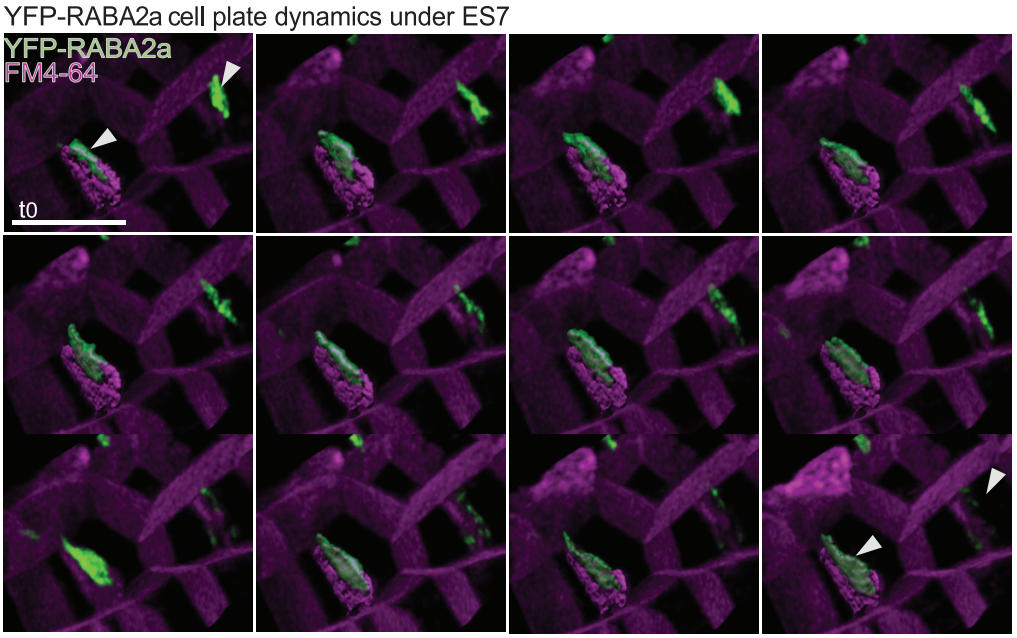

Fig. 4. YFP–RABA2a cell plate dynamics under Endosidin 7 (ES7) treatment. YFP–RABA2a (green) vesicle accumulation and FM4-64- (purple) stained plasma membrane show cell plate development under ES7 treatment. Note the abnormal pattern and the fragmentation of the cell plate as it transitions during different time points. The pattern of YFP–RABA2a at the cell plate periphery does not expand radially, as seen in the untreated plants. Further, the cell plate cannot follow normal maturation into membranes detectable with FM4-64. Data were collected on a Leica SP8. Scale bar=10 μm. Δ*t*=1.5 min.

under ES7 treatment. Thus, we again employed LLSM. The use of LLSM still allowed imaging of various cytokinetic events, facilitating quantification and providing an analysis of the impact of callose inhibition. It is worth noting that the observed events took longer compared with untreated plants.

In contrast to the untreated seedlings (Fig. 3), the cell plates subjected to a 2 h ES7 pulse treatment (Fig. 5) exhibited a notable accumulation of YFP–RABA2a volume that persisted beyond 15 min without significant expansion in the cell plate itself. Meanwhile, the marker maintained a condensed structure, eventually fragmenting throughout the lifetime of the imaged cell plates (Fig. 5A; Supplementary Video S2, cell plates shown in blue). Another ES7-induced phenotype, though less frequent, showed relative expansion in the cell plate, but also eventually fragmented in an erratic pattern (shown in pink in Supplementary Video S3). Overall, the relative expansion did not match that observed in untreated samples, as further discussed below. Under the influence of ES7, the attempted cell plate development ran longer than in the controls, averaging 35 ± 13.7 min compared with the 20–30 min in untreated samples. The variation in ES7-induced phenotypes was probably due to the timing of the drug's effect at different cytokinetic stages, as multicellular root tips are not synchronized.

Quantifying YFP–RABA2a cell plate volumes (Fig. 5B) and their corresponding rates of change (Fig. 5C) under a 2 h ES7 pulse treatment showed an initial phase of rapid volume growth, followed by a slower to stagnant accumulation of YFP–RABA2a membrane material, leading to a plateau of retained volume over a longer time frame. This prolonged plateau contributes to the increased average division time compared with the untreated plants (Fig. 5B, C). Similarly, the bounding surface area of the cell plates exhibited very similar dynamics and behavior, with a broad plateau of surface area over time and a severely depressed rate of surface area change (Fig. 5D, E). Overall, the phenotypic observations and quantifications of cell plate characteristics demonstrate a stark difference between ES7-treated and control cell plates. While the control cell plates followed distinct, consistent growth phases based on volume changes, marked by a transition from positive to negative rates, no apparent pattern changes in ES7-treated volumes, corresponding to discernible phase transitions, were observed.

In order to assess the impact of ES7, the volume growth rates of both control and ES7-treated cell plates were divided into equidistant volume intervals using 20% intervals (six 'bins') for statistical analysis. We focused on five bins, as the sixth bin at the end of the collection showed high variability. The first three intervals (bins 1–3) correspond to the normalized increasing volumes in the control, ranging from 0 to 0.33 μm^3, 0.33 μm^3 to 0.66 μm^3, and 0.66 μm^3 to 1 μm^3, respectively. Intervals 4 and 5 represent reducing volumes ranging between 1 μm^3 and 0.66 μm^3 and between 0.66 μm^3 and 0.33 μm^3, respectively (Fig. 6F). Bin 1 (Fig. 6A) corresponds to the interval with maximum volume accumulation, which is similar between the control and ES7 (Figs 3, 5). Intervals 2, 3, and 5 exhibited statistically significant differences between the control and ES7 treatments (Fig. 6B–C,

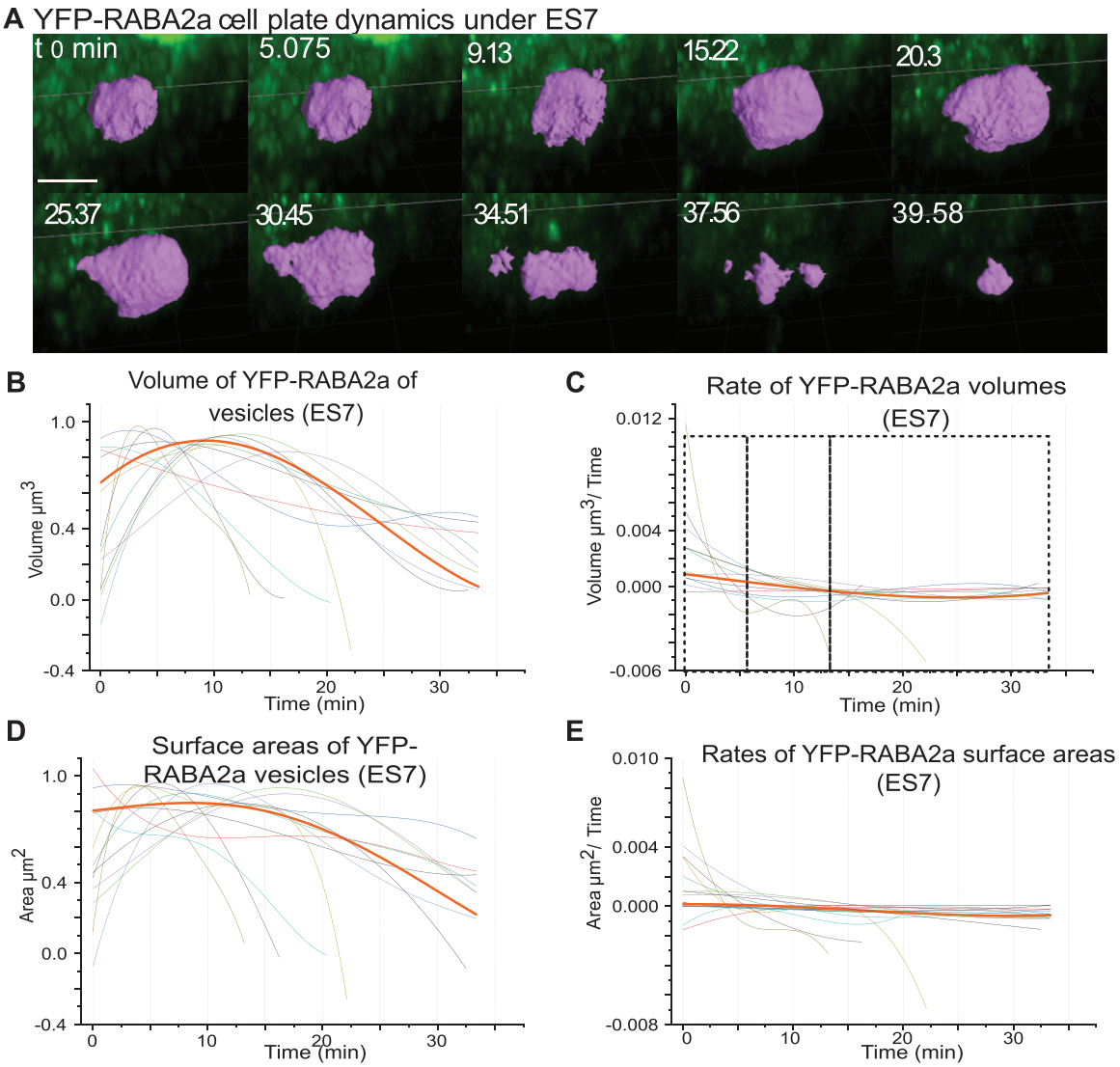

Fig. 5. Quantitative YFP–RABA2a dynamics at the cell plate under ES7 treatment. (A) Representative snapshots of a time series showing the YFP–RABA2a segmented cell plate transition under ES7 treatment. The segmented cell plate is shown in purple from its first emergence, not able to expand radially and flatten. (B–E) Volumes and bounding surfaces of segmented cell plates and their rates of change. Each line indicates an individually segmented cell plate. Note that the cell plate shown in (A) is highlighted in bold in all graphs. Normalized volumes and bounding surface areas of developing cell plates were fitted to a polynomial distribution (B and D). First-degree derivatives present the corresponding rates of change of the polynomial fits for the volume and the bounding surface area, respectively (C and E). Scale bar=10 µm. *n*=18.

E). The most pronounced difference was observed in interval 5 (Fig. 6E), in which ES7-treated cell plates showed minimal growth reduction and maintained a positive average rate, in contrast to the non-treated plates. Notably, the maximum amount of volume or bounding surface area accumulated by YFP–RABA2a throughout all the events was not statistically different between ES7 and controls (Supplementary Fig. S3), indicating that vesicle accumulation remains unaffected by the inhibition of callose. Taken together, the data suggest that inhibition of cytokinetic callose disrupts the phase transition from cytokinetic vesicle/volume accumulation to volume reduction and cell plate maturation.

Expansion rate analysis identifies a critical point for callose deposition

Prior models have relied on radial expansion to stage cell plate maturation, using confocal microscopy data (Higaki *et al*., 2008; van Oostende-Triplet *et al*., 2017). To gain deeper insights into the morphological stages of cell plate development and how they are impacted by callose inhibition, we also adopted the cell plate diameter as a measure of expansion (Fig. 7; Supplementary Fig. S4). At each time point, we measured the diameter at the longest distance across the outermost opposing edges of detectable YFP–RABA2a at the cell plate's

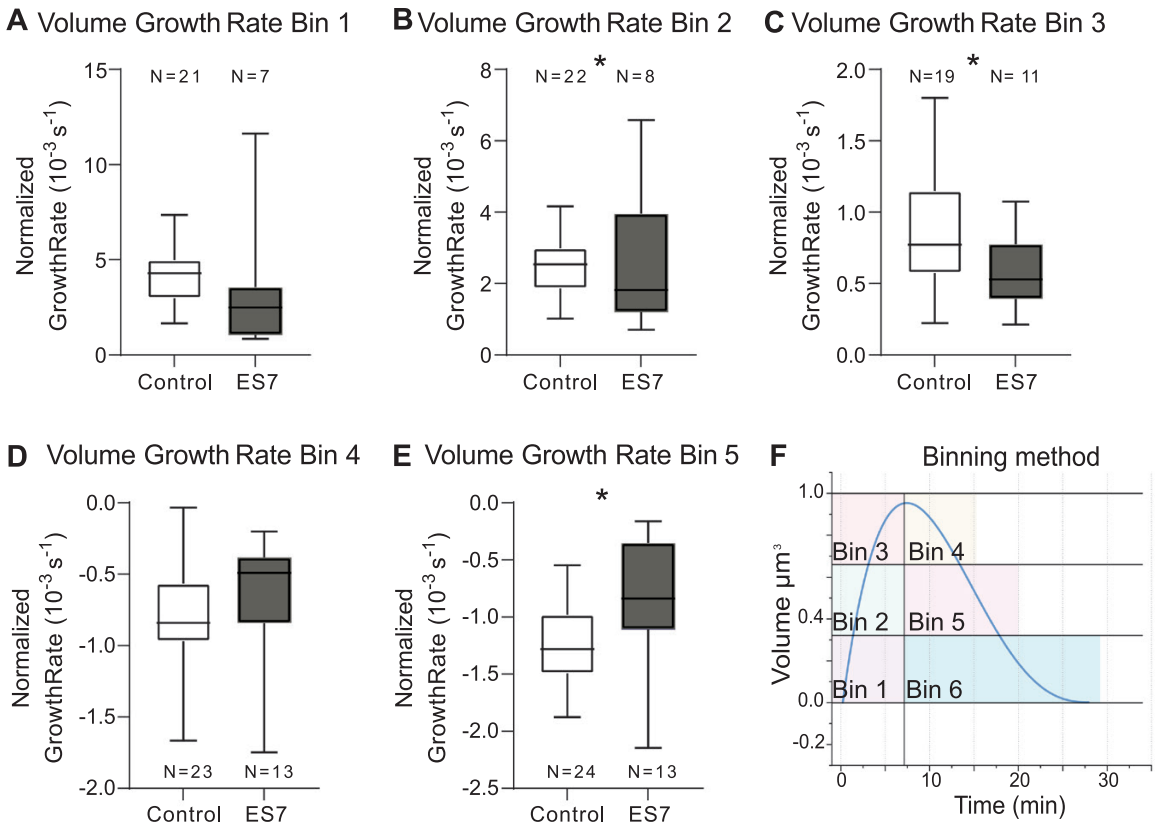

Fig. 6. Statistical comparison of volume accumulation. YFP–RABA2a normalized volume growth rates, averaged within pre-defined groups and shown with 95% confidence intervals. (A–C) Bins 1–3 represent the rates corresponding to normalized volumes increasing from 0 to 0.33 µm^3, 0.33 µm^3 to 0.66 µm^3, and 0.66 µm^3 to 1 µm^3, respectively. All bins correspond to the first derivative rates of volume growth. *Indicates P<0.005. (D and E) Bins 4 and 5 represent the rates corresponding to volumes decreasing from 1 µm^3 to 0.66 µm^3 and from 0.66 µm^3 to 0.33 µm^3, respectively; bin 6 data are not shown due to the bin spanning over the region in which the end of collection has limited control over noise. All bins correspond to the first derivative rates of volume growth. *Indicates P<0.005. (F) Schematic representation of volume growth grouped in bins for further processing as shown in (A–E).

rim, using the FM4-64 plasma membrane stain to determine the predicted final cross-wall width, and normalized the diameters, accounting for cell size variations (Chow *et al.*, 2008; van Oostende-Triplet *et al.*, 2017). The diameter analysis (Fig. 7A; Supplementary Fig. S4A, B) displayed a logarithmic expansion pattern in control plants. In contrast, the ES7-treated plants exhibited unstable growth with a reduction trend observed after 10–12 min (Fig. 7A; Supplementary Fig. S4C, D). These findings provide valuable insights into the effect of callose inhibition on cell plate development and its impact on the expansion dynamics of the cell plates.

Interestingly, during the first 8–10 min that marked the bulk of vesicle volume accumulation, both ES7-treated and control cell plates reached the same expansion levels corresponding to ~60% of the predicted final diameter. While control cell plates continued growing exponentially, ES7-treated cell plates showed minimal expansion beyond the first 10 min (Fig. 7A). Based on these data, the intersection of the two growth curves indicates a critical point at which callose is essential for cell plate expansion. Notably, this time interval corresponds to the cell plate phase transition from phase I to phase II, during which volume growth changes from a positive to a negative rate and a significant volume loss occurs (Fig. 3B, C).

Our previously developed biophysical model highlights the importance of a spreading force, probably by the deposition of callose, for a cell plate to transition from a vesicular membrane network to a fenestrated sheet and finally to a mature cell plate (Jawaid *et al.*, 2022). Combined with the presented data, we hypothesize that cell plate formation is characterized by a distinct, callose-dependent transition that changes from membrane accumulation to membrane recycling within ~10 min. We suppose that some ES7-treated cell plates achieve a considerable level of expansion, probably due to the timing of the treatment. However, the majority tend to collapse or fragment, and fail to reach the parental cell wall.

There were significant technical difficulties in reliably measuring the thickness of the somewhat irregular cell plates, which led us to use the cell plate volume divided by the bounding cell plate surface to estimate plate thickness. The volume-to-bounding surface area ratio in control cell plates shows a bell curve distribution (Fig. 7B), with an initial volume accumulation phase followed by flattening,

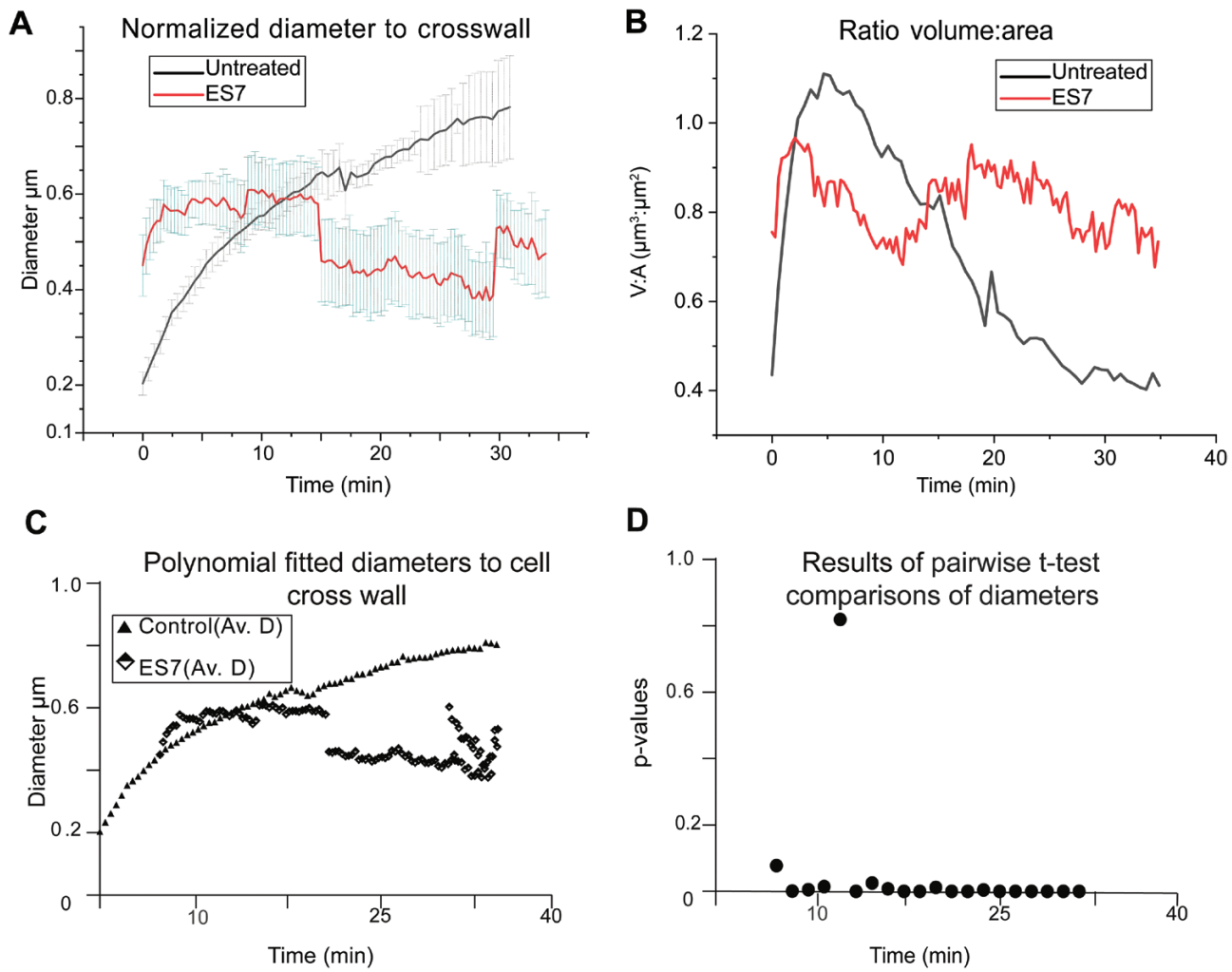

Fig. 7. Cell plate diameter expansion under control and Endosidin 7 (ES7) treatment. Cell plate transition based on cell plate diameter expansion under control and ES7 treatment. (A) Control cell plates show a logarithmic expansion pattern, while ES7 treatment causes a more level pattern. Cell plate diameters are normalized to the expected cross-wall length. Note the intersection between control and ES7 treatment, indicating a critical point for cell plate maturation. (B) Volume-to-bounding surface area ratio in control and ES7-treated cell plates. The average of the ratio for cell plates analyzed in Figs 3 and 5 are shown. Control *n*=23, ES7 *n*=12. (C) Polynomial fit was applied to cell plate diameters that have been normalized to the corresponding cross-wall. (D) Results of pairwise *t*-test comparisons along moving averages shown in (C). Analysis shows that all except one time point are statistically different on cell plate expansion when comparing control with the absence of callose via ES7 treatment. Non-treated *n*=24, treated *n*=18.

thinning, and diametric expansion of the cell plate. However, when treated with callose-inhibiting ES7, the volume-to-bounding surface ratio followed a fluctuating flat line without a significant volume loss (Fig. 7B). This behavior might be indicative of a mechanism that critically inhibits 'radial' expansion and potential redistribution/recycling of membrane material. Polynomial fitted cell plate diameters were grouped into 20 intervals (bins) which were subjected to statistical analysis comparing control versus ES7-treated cell plates (Fig. 7C). All but one interval was statistically different (Fig. 7D; Supplementary Fig. S4E). Notably, this one interval identifies the intersection of the ES7 and control cell plate expansion curves and is a critical point in which callose's presence is essential.

Callose deposition appears in the late cytokinetic stages

Next, we examined the localization of callose in relation to YFP–RABA2a to test if its presence corresponds to the predicted critical point during cell plate expansion. Using the callose-specific stain aniline blue fluorochrome (Evans and Hoyne, 1982) and employing multichannel live cell imaging, we characterized the transient presence of callose in relation to the cytokinesis marker YFP–RABA2a. During the early stages of cell plate development, no callose signal was identified (Fig. 8A), while significant YFP–RABA2a accumulation was observed, marking an expanding cell plate. During later stages of cell plate development, callose was clearly

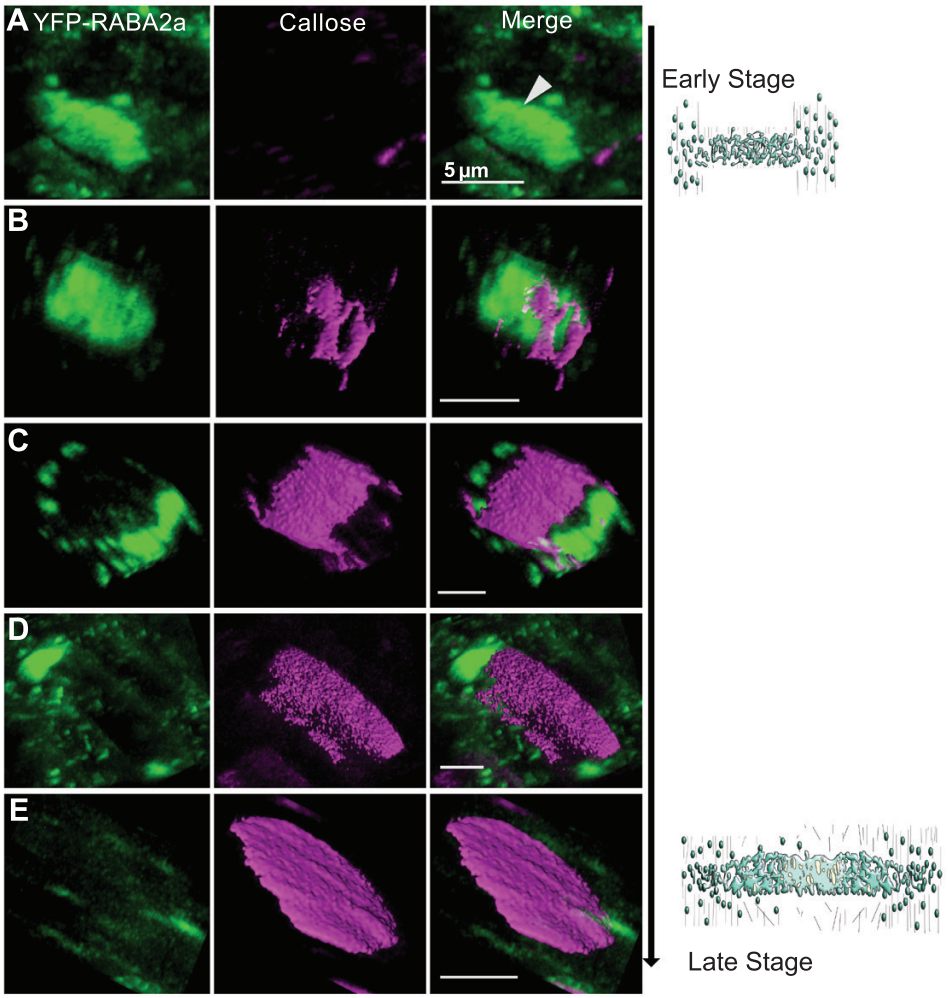

Fig. 8. Progression of the cell plate in the presence of callose. (A–E) Cell plate development in the presence of callose. (A) An early-stage cell plate before the accumulation of callose. At this stage, only vesicle accumulation by YFP–RABA2a (green) makes up the cell plate. (B–D) Later stage cell plates where callose accumulation stained with aniline blue fluorochrome (magenta) is detectable. Note the transient accumulation of callose in later stages, leading to the maturation of the cell plate during normal cytokinesis. (B) Initial callose deposition overlapping with YFP–RABA2a. (C) As the cell plate maturation continues and the YFP–RABA2a accumulation takes a 'doughnut shape' pattern, callose deposition appears in the middle of the cell plate with minimal overlap with YFP–RABA2a at the leading edge. (D) Callose is present throughout the cell plate, while minimal YFP–RABA2a is shown at the discontinuous ring (E). Mature cell plate predominately labeled by callose. Scale bar=5 µm.

identifiable and spatially distinct from YFP–RABA2a. The cytokinetic vesicle marker YFP–RABA2a showed a ring or partial ring pattern (Fig. 8C, D), while callose was observed in an expanded disk form (Fig. 8C–E). We observed callose deposition beginning at this critical morphological transition point corresponding to the ~8–10 min mark characterized by a change from a disk-shaped to a ring-shaped YFP-–RABA2a pattern. We conclude that the polysaccharide is deposited during the transitional stages of YFP–RABA2a volume reduction and cell plate expansion. This pattern distinctly corresponds to phases II and III and covers the interval beyond the crossover point predicted by cell plate diameter expansion.

Discussion

Mitosis, being the fundamental process of life that drives growth and development, necessitates a deeper understanding of its intricate details and complexity. Thus, the ability to image cytokinesis at a high spatiotemporal level is of immense value in advancing developmental biology. In plants, cytokinesis is unique as it involves the *de novo* formation of a cell plate that expands centrifugally, leading to the separation of two daughter cells. The dynamic nature of various cell plate development stages that occur simultaneously demands sensitive imaging techniques with minimal photobleaching to comprehensively capture the entire process. Although electron tomography

studies have contributed significantly to our current knowledge of cytokinesis (Samuels *et al*., 1995; Seguí-Simarro *et al*., 2004), they lack the ability to provide consecutive time points in the same sample, limiting their capacity for robust statistical analysis. Moreover, conventional laser scanning confocal microscopy, despite its excellent lateral, axial, and temporal resolution, is too photo-damaging to conduct high-quality, extended time-lapse acquisitions.

The development of LLSM affords imaging at much faster rates, with less light exposure of the sample, minimizing photobleaching and phototoxic effects, which extends the observation time, while affording higher axial resolution and maintaining near confocal microscopy-type lateral resolutions (Chen *et al*., 2014). In this context, LLSM allows the collection of previously unobtainable datasets to dissect mitosis. Taking advantage of the resolution, speed, and gentle illumination, LLSM has been used to dissect mitosis and endomembrane dynamics in a variety of systems, including single cells in culture, *Caenorhabditis elegans*, zebrafish (Chen *et al*., 2014; Aguet *et al*., 2016), and human cells (Sen *et al*., 2021), providing new insights into cell division and its regulatory processes. The plant research community is slowly embracing the benefits that light sheet microscopy and vertical imaging offer (Vyplelová *et al*., 2017; Glanc *et al*., 2018; Ovecka *et al*., 2022). In plants, apart from root hair studies (Tichá *et al*., 2020; Ovecka *et al*., 2022), the potential of LLSM has not been explored to understand regulatory mechanisms in cytokinesis. A likely factor is the still limited availability of the instrumentation and the substantial effort needed in the post-processing and quantitative analysis.

Further, given that plant cell walls can introduce aberrations in super-resolution imaging methods (Chatterjee *et al*., 2018; Novák *et al*., 2018; Ovecka *et al*., 2022), performance of LLMS is understandably a potential concern when imaging plants. This study, however, illustrates the feasibility and power of LLSM for attaining hitherto unobtainable detailed spatio-temporal data in plants over time periods of 30–40 min on a whole organismal level and within a biologically relevant context. Volume imaging at ~25–30 s time intervals allowed a detailed view of cell plate transition stages with high enough quality to segment and quantify at a biologically relevant scale. High imaging frequency is particularly exciting and valuable when observing transient events that appear somewhat randomly and unpredictably, such as cell plate formation within the intact root tip. The ability to capture complete (temporally and spatially) sporadic events embedded within plant tissue with sufficient resolution and in statistically significant numbers represents a major step forward in methodology and an opportunity for experimentation.

Cell plate volume behavior follows three distinct and consistent phases

Our robust cytokinetic YFP–RABA2a vesicle volume analysis during the entire process of cytokinesis showed distinct behavioral patterns that allowed the identification of three phases based on volume growth patterns. We attempt to assign previously structurally described cell plate development stages (Samuels *et al*., 1995) to the identified phases.

(i) Phase I is characterized by a positive volume accumulation rate that peaks at ~7–10 min before reaching an inflection point, representing the initial cell plate biogenesis stage. Our analysis showed a relative diameter increase of 50–60% of the parental cell width during phase I. The vesicle fusion, tubular vesicular network (FVS, TVN), and some tubular network (TN) transitions (Samuels *et al*., 1995) are probably included in this phase that corresponds to the delivery and fusion of cytokinetic vesicles at the cell plate edge and membrane network formation at the core of the cell plate disk.

(ii) Phase II, transitioning through an easily identifiable inflection point, is characterized by a negative volume growth rate with rapid loss reaching a minimum within ~15 min. We reason that during this phase, representing a ring phragmoplast stage, the center of the cell plate has transitioned to a fenestrated sheet (PFS) (Samuels *et al*., 1995), requiring massive membrane recycling (Seguí-Simarro *et al*., 2004). The observed recycling is consistent with earlier predictions estimating a 75% membrane reduction during cell plate maturation in endosperm cellularization (Otegui *et al*., 2001). The cell plate during this phase reaches almost 70–80% of the final cell plate diameter.

(iii) Phase III, marked by the remaining period of cell plate development, is characterized by a minimal but stable positive volume growth rate. The overall return to net positive growth probably represents PFS structures (Samuels *et al*., 1995; Seguí-Simarro *et al*., 2004) associated with a discontinuous phragmoplast with minimal cytokinetic vesicle delivery, leading to the final expansion and maturation of the cell plate until it fuses with the parental cell wall.

Because cell plate development encompasses several stages that occur simultaneously in each phase, recycling of excess membrane material may already begin during phase I; however, based on the vast vesicle delivery, the net rate is positive, contrasting with phase II, dominated by membrane recycling and a net negative volume growth rate. Phase III requires minimal membrane addition but stabilization and maturation of the cell plate, thus reverting to a net positive volume growth rate. The minimal net positive increase could be due to the reorganization of the cell plate membrane at the edge, as it needs to combine with the parental plasma membrane carrying the targeted and necessary machinery and cargo for joining with the parental cell wall.

Earlier models based on cell plate diameter suggest a gradual decrease in cell plate expansion rates (Higaki *et al*., 2008) or a biphasic pattern (van Oostende-Triplet *et al*., 2017) as the cell plate expands towards the parental wall. The model of van Oostende-Triplet *et al*. identifies a primary centrifugal growth

(PCG) phase in BY-2 cells with an average diameter growth rate of 1.44 ± 0.44 μm min^{-1} and a secondary centrifugal growth (SCG) phase with a rate of 0.35 ± 0.13 μm min^{-1}, along with similar estimates in Arabidopsis (PCG ~0.87 ± 0.26 μm min^{-1}, SCG ~0.25 ± 0.09 μm min^{-1}) (van Oostende-Triplet *et al.*, 2017). Analysis of our diameter expansion data, as guided by the YPF–RABA2a marker, showed an initial high growth rate of 4.09 ± 0.26 μm min^{-1} followed by a gradual decrease, which can be grouped in two bins that average 1.1 ± 0.05 μm min^{-1} and 0.59 ± 0.04 μm min^{-1} (n=18) (Supplementary Fig. S5A), consistent with the earlier calculated rates described above (van Oostende-Triplet *et al.*, 2017). The extremely rapid expansion rate within the first 2.5 min of cell plate development (Supplementary Fig. S5B, C) aligns with cell plate biogenesis during vesicle delivery. It corresponds to the initial plate assembly (IPA) stage postulated by van Oostende-Triplet *et al.* (2017), for which expansion rates were not detectable. Taken together, this is a clear example of LLSM enabling the recording of cell plate biogenesis and the calculation of the corresponding rates, as it can capture early events prior to well-defined cell plate appearance in the field of view.

It is apparent in comparing different models that understanding cell plate development based on volumetric growth provides more straightforward cut-off points for phase transitions and complements cell plate diameter analysis. Proof of this concept is demonstrated in this study with the volume accumulation rates of the easily trackable cytokinesis marker. This analysis allows the prediction of quantitative behaviors during cell plate development and their interrogation to understand the contribution of different components. For example, models of phragmoplast expansion (Higaki *et al.*, 2008) can be tested, similarly to what was done here, to evaluate the contributions of the array that helps build the cell plate. The easily identifiable inflection points between phases mark critical points during the transition of the membrane network and cell plate expansion that requires the onset of specific contributing factors. We propose that during the transition from phase I to II, clathrin-mediated recycling is enhanced, and that polysaccharide deposition and assembly are dominant during the transition from phase II to III. Future studies can leverage the method and explore the proposed model to interrogate different markers such as clathrin, dynamin, and SNARE proteins involved in different aspects of cell plate development. It is plausible that the volumetric-based transitions will vary based on the marker used, for example SNARE versus clathrin (Bednarek and Backues, 2010; El Kasmi *et al.*, 2013; Jürgens *et al.*, 2015; Dahhan and Bednarek, 2022; Park *et al.*, 2023), which will help to build more comprehensive models.

Callose is necessary during cell plate expansion for the transition beyond phase I

An example of how the current analysis and proposed model can provide insights into cell plate development is the contribution of callose, a polysaccharide transiently deposited during cell plate development. The specific stage at which callose plays a critical role has long been debated, with views arguing on either the transition from a TN to PFS or the cell plate insertion in the parental cell wall (Samuels *et al.*, 1995; Thiele *et al.*, 2009). Different methods to dissect its role, direct detection of callose with antibodies against the polysaccharide with electron microscopy (Samuels *et al.*, 1995) versus confocal 2D staining and mutant characterization (Thiele *et al.*, 2009), might contribute to this difference. The developed approach and the derived model here, in combination with pharmacological treatment, allow the detailed dissection of each stage, providing insights into the biological role of the polymer. Upon inhibition of callose with ES7, phase I is prolonged. An irregular pattern is seen following the initial phase, with no distinguishable phase II and III. This clearly illustrates that the polysaccharide is essential during the transition beyond phase I.

A modeling approach was previously implemented to understand better the cell plate stage transition from a vesicular network to a fenestrated sheet and mature cell plate. The model predicts that the onset of a 2D spreading/stabilizing force, coupled with a concurrent loss of spontaneous curvature, is necessary for cell plate expansion (Jawaid *et al.*, 2022). Biophysical modeling highlights the need for a spreading force during the transition of the membrane network (TN) to a fenestrated sheet (PSF) (Jawaid *et al.*, 2022), which overlaps with the phase transition (phase I to phase II) in our study. Directly detecting callose via fluorescent staining corresponding to these phases validates the prediction of the biophysical model. Callose, due to its amorphous structure, can lead to alterations in the physical and mechanical properties at the deposition site (Piršelová and Matušíková, 2013; Zhang *et al.*, 2021; Ušák *et al.*, 2023). The polysaccharide has the ability to enhance rigidity while maintaining flexibility and to reduce permeability to various compounds across a range of functions (Yim and Bradford, 1998; Parre and Geitmann, 2005; Vatén *et al.*, 2011). Additionally, callose's unique composition compared with other polysaccharides enables controlled degradation when no longer necessary, underlining its significance as a compound that can operate both spatially and temporally (Samuels *et al.*, 1995; Ušák *et al.*, 2023).

Lattice light sheet microscopy along with 4D volume-based phase transition analysis is robust for cytokinesis dissection

The quantitative prediction of phase transitions, with unbiased characterization, provides an advantage over descriptive interpretations of fragmented datasets. Further, it establishes a roadmap into which other components can be incorporated. Structural cell wall proteins, such as extensins (Cannon *et al.*, 2008), wall matrix polysaccharides (Moore and Staehelin, 1988), cellulose (Miart *et al.*, 2014), and other forms of linear glucose can be

interrogated with the same analysis methodology. Cellulose, the load-bearing cell wall polysaccharide, is a prime candidate for this analytical approach, especially in combination with conditional genetic mutations or pharmacological inhibition of cellulose synthases (Chen *et al.*, 2018). Interestingly, a 5 d inhibition of cellulose synthase activity with isoxaben causes reduction of cell elongation but does not have a prominent effect on cell plate biogenesis or expansion (Jawaid *et al.*, 2022), which suggests a role for cellulose in the formed cell wall instead of cell plate expansion. A quantitative analysis during cell plate phase transition can help dissect the contribution of cellulose or other linear β-1,4-glucans. Beyond cellulose synthase, cellulose synthase-like proteins (CSLs), such as CSLD3, produce linear glucan polymers (Yang *et al.*, 2020). CSLD5, a cytokinesis-specific protein (Gu *et al.*, 2016), produces a β-1,4-glucan polysaccharide, similar to that produced by CSLD3 (Yang *et al.*, 2020). Adaptation of our quantitative analysis in conditional mutations of these proteins might pin down the specific contributions to cell plate development and indicate associations with other polysaccharides or cell wall components. Such a study can address the potential interaction of CSLD5 products with callose in creating a scaffold (Abou-Saleh *et al.*, 2018) for the establishment of the spreading force necessary for cell plate maturation.

While our study was centered on callose, the described model of cytokinetic vesicle behavior can be interrogated for an array of contributions to cell plate development (Smertenko, 2018; Cheng and Bezanilla, 2021; Dahhan and Bednarek, 2022; Gu and Rasmussen, 2022; Sinclair *et al.*, 2022; Lebecq *et al.*, 2023; Nan *et al.*, 2023; Park *et al.*, 2023), for example pharmacological inhibition of secretory traffic, cytoskeleton dynamics at the phragmoplast, and its interaction with vesicle delivery. In a recent study, the application of the Small Molecular Inhibitor Formin Homology 2 (SMIFH2) revealed the function of formins in several aspects of cytokinesis, including cell plate membrane organization, microtubule polymerization, and nucleating F-actin at the cell plate (Zhang *et al.*, 2021). The application of LLSM and the methodology developed here can aid in further dissecting the role of formins in cell plate development and phragmoplast organization. The pharmacological inhibition of actin or microtubule polymerization has been extensively used to study phragmoplast expansion and was recently employed for cell plate development studies using a radial expansion model (van Oostende-Triplet *et al.*, 2017). Extending these studies to a 4D analysis based on rates of volume accumulation can provide extra depth, allowing for direct correlations of the contributions of cytoskeleton dynamics, secretory traffic, and protein synthesis in cell plate biogenesis and expansion.

Conclusion

The development of a comprehensive 4D image acquisition and processing pipeline using LLSM represents an important step forward in both utilizing cutting-edge microscopy tools and addressing long-standing questions about spatiotemporal dynamics in cytokinesis. Despite the advantages, today LLSM-based imaging of plant seedlings is still limited. The current approach requires genetically encoded fluorophores with high photostability, thus not all markers are ideally suited. Multiplex imaging of different fluorophores may be impacted by crosstalk and requires multichannel camera systems. Another major challenge is the substantial data size generated during the image analysis and archiving. For instance, the current study produced ~40 TB of data, which poses significant demands on Information technology (IT) infrastructures for processing and storage. However, it is important to highlight a distinctive feature of this experimental design—the ability to conduct prolonged imaging over a large field of view.

The developed 4D imaging pipeline using LLSM, along with the tools for processing the acquired images, are documented and are available through plugins in ImageJ and MATLAB. The segmentation pipeline employed in Imaris is also documented for easy adaptation (Fig. 2). The cell plate development model can be applied using different modalities beyond LLSM to dissect plate cytokinesis. We hope that this study inspires the community to adopt the methodology of exploring LLSM in plants, take advantage of the image analysis pipeline tools developed, and refine the model of cell plate development and its factors contributing to each phase.

More importantly, our study was able to showcase first-of-its-kind data of the complete process of cell plate development with minimal photobleaching, higher axial resolution, and faster imaging rates compared with traditional laser scanning confocal microscopy. The study revealed three distinct developmental phases of cell plate growth, from rapid vesicle accumulation to subsequent volume reduction and cell plate expansion, and the critical role of callose in the phase transition. The use of the chemical inhibitor ES7 in combination with LLSM provided quantitative insights into the timing and role of callose in stabilizing the cell plate during expansion and maturation. Inhibition of callose deposition led to impaired cell plate expansion, resulting in fragmented and aberrant membrane accumulation patterns. The findings of this study have significant implications for understanding the spatiotemporal dynamics of cell plate development and the role of callose along with other components in this process.

We see this pioneering effort in quantitative dissection of cell plate development helping to understand the array of factors controlling plant cytokinesis. Taken together, this research contributes to the broader understanding of plant cell biology and suggests new avenues for further investigations into the molecular mechanisms underlying cell plate assembly and expansion.

Supplementary data

The following supplementary data are available at *JXB* online.

Fig. S1. Quantitative YFP–RABA2a dynamics and FM4-64-stained membrane accumulation at the cell plate.

Fig. S2. Representative morphologies of ES7-induced arrested development of cell plate growth.

Fig. S3. Maximum accumulation of volume and bounding surface area across treatments.

Fig. S4. Expansion rates of individual cell plates based on their radial growth.

Fig. S5. Comparison of expansion trends based on diameter or volume.

Fig. S6. Overlay of polynomial fit to YFP–RABA2a segmented volume over time.

Table S1. Quantitative data used for untreated cell plate analysis.

Table S2. Quantitative data used for ES7 pulse-treated cell plate analysis.

Table S3. Quantitative data used for cell plate analysis as described in Supplementary Fig. S1.

Video S1. 4D rendering of YFP–RABA2a cell pate accumulation with surface segmentation. Images were acquired with LLSM.

Video S2. 4D rendering of YFP–RABA2a cell pate accumulation with surface segmentation under 2 h treatment with 50 μM ES7 displaying relatively no expansion. Images were acquired with LLSM.

Video S3. 4D rendering of YFP–RABA2a cell pate accumulation with surface segmentation under 2 h treatment with 50 μM ES7 displaying minimal relative expansion. Images were acquired with LLSM.

Acknowledgements

This manuscript is dedicated in memory of Professor Andrew Staehelin whose work and contribution to the field inspired us in this study. We want to thank all the members of AIC and the Drakakaki lab for their input, and Dr Destiny J. Davis for her critical reading of the manuscript.

Author contributions

TW and GD: conceptualization and supervision; RMS, MW, MZJ, TW, and GD: methodology; RMS, TW, MZJ, DC, and JH: formal analysis; GD, RMS, TW, MW, and TL: investigation; KMD, TW, and GD: resources; RMS, TW, and GD: data curation; RMS, TW, and GD: writing—original draft; RMS, TW, MW, MZJ, DC, and GD: writing—review & editing; RMS, TW, and MZJ: validation; RMS, JA, KMD, JH, TW, and GD: visualization; MZJ, BR, EW, KMD, and JH: software; GD: project administration; DC and GD: funding acquisition.

Conflict of interest

The authors declare no competing interests.

Funding

This work was supported by National Science Foundation Grant MCB 1818219 to GD and DC. GD was additionally partially supported by the US Department of Agriculture Hatch (CA-D-PLS-2132-H). RS acknowledges the Department of Plant Sciences, UC Davis for the award of a GSR scholarship funded by endowments, particularly the McDonald Endowment, administered by UCANR and the DEB fellowship. We acknowledge the NIH award 1S10OD026702-01 that was used to purchase the Zeiss 980 laser scanning confocal microscope.

Data availability

Representative datasets used in the study are available on Zenodo: https://doi.org/10.5281/zenodo.10515765 (Sinclair *et al.*, 2024)

References

Abou-Saleh RH, Hernandez-Gomez MC, Amsbury S, *et al*. 2018. Interactions between callose and cellulose revealed through the analysis of biopolymer mixtures. Nature Communications **9**, 4538.

Aguet F, Upadhyayula S, Gaudin R, *et al*. 2016. Membrane dynamics of dividing cells imaged by lattice light-sheet microscopy. Molecular Biology of the Cell **27**, 3418–3435.

Bednarek SY, Backues SK. 2010. Plant dynamin-related protein families DRP1 and DRP2 in plant development. Biochemical Society Transactions **38**, 797–806.

Berson T, von Wangenheim D, Takáč T, Šamajová O, Rosero A, Ovečka M, Komis G, Stelzer EHK, Šamaj J. 2014. Trans-Golgi network localized small GTPase RabA1d is involved in cell plate formation and oscillatory root hair growth. BMC Plant Biology **14**, 252.

Cannon MC, Terneus K, Hall Q, Tan L, Wang Y, Wegenhart BL, Chen L, Lamport DTA, Chen Y, Kieliszewski MJ. 2008. Self-assembly of the plant cell wall requires an extensin scaffold. Proceedings of the National Academy of Sciences, USA **105**, 2226–2231.

Chatterjee K, Pratiwi FW, Wu FCM, Chen P, Chen BC. 2018. Recent progress in light sheet microscopy for biological applications. Applied Spectroscopy **72**, 1137–1169.

Chen BC, Legant WR, Wang K, *et al*. 2014. Lattice light-sheet microscopy: imaging molecules to embryos at high spatiotemporal resolution. Science **346**, 1257998.

Chen HW, Persson S, Grebe M, McFarlane HE. 2018. Cellulose synthesis during cell plate assembly. Physiologia Plantarum **164**, 17–26.

Chen XY, Liu L, Lee EK, Han X, Rim Y, Chu H, Kim SW, Sack F, Kim JY. 2009. The *Arabidopsis* callose synthase gene GSL8 is required for cytokinesis and cell patterning. Plant Physiology **150**, 105–113.

Cheng X, Bezanilla M. 2021. SABRE populates ER domains essential for cell plate maturation and cell expansion influencing cell and tissue patterning. eLife **10**, e65166.

Chow CM, Neto H, Foucart C, Moore I. 2008. Rab-A2 and Rab-A3 GTPases define a trans-Golgi endosomal membrane domain in *Arabidopsis* that contributes substantially to the cell plate. The Plant Cell **20**, 101–123.

Dahhan DA, Bednarek SY. 2022. Advances in structural, spatial, and temporal mechanics of plant endocytosis. FEBS Letters **596**, 2269–2287.

Desprez T, Juraniec M, Crowell EF, Jouy H, Pochylova Z, Parcy F, Höfte H, Gonneau M, Vernhettes S. 2007. Organization of cellulose synthase complexes involved in primary cell wall synthesis in *Arabidopsis thaliana*. Proceedings of the National Academy of Sciences, USA **104**, 15572–15577.

Drakakaki G. 2015. Polysaccharide deposition during cytokinesis: challenges and future perspectives. Plant Science **236**, 177–184.

Drakakaki G, Robert S, Szatmari AM, *et al*. 2011. Clusters of bioactive compounds target dynamic endomembrane networks in vivo. Proceedings of the National Academy of Sciences, USA **108**, 17850–17855.

El Kasmi F, Krause C, Hiller U, Stierhof YD, Mayer U, Conner L, Kong L, Reichardt I, Sanderfoot AA, Jürgens G. 2013. SNARE complexes of

different composition jointly mediate membrane fusion in *Arabidopsis* cytokinesis. Molecular Biology of the Cell **24**, 1593–1601.

Evans NA, Hoyne PA. 1982. A fluorochrome from aniline blue: structure, synthesis and fluorescence properties. Australian Journal of Chemistry **35**, 2571–2575.

Geitmann A. 2023. Seeing clearly—plant anatomy through Katherine Esau's microscopy lens. Journal of Microscopy **291**, 92–104.

Geldner N, Dénervaud-Tendon V, Hyman DL, Mayer U, Stierhof YD, Chory J. 2009. Rapid, combinatorial analysis of membrane compartments in intact plants with a multicolor marker set. The Plant Journal **59**, 169–178.

Glanc M, Fendrych M, Friml J. 2018. Mechanistic framework for cell-intrinsic re-establishment of PIN2 polarity after cell division. Nature Plants **4**, 1082–1088.

Gu F, Bringmann M, Combs JR, Yang J, Bergmann DC, Nielsen E. 2016. *Arabidopsis* CSLD5 functions in cell plate formation in a cell cycle-dependent manner. The Plant Cell **28**, 1722–1737.

Gu Y, Rasmussen CG. 2022. Cell biology of primary cell wall synthesis in plants. The Plant Cell **34**, 103–128.

Higaki T, Kutsuna N, Sano T, Hasezawa S. 2008. Quantitative analysis of changes in actin microfilament contribution to cell plate development in plant cytokinesis. BMC Plant Biology **8**, 80.

Jawaid MZ, Sinclair R, Bulone V, Cox DL, Drakakaki G. 2022. A biophysical model for plant cell plate maturation based on the contribution of a spreading force. Plant Physiology **188**, 795–806.

Jürgens G. 2005. Cytokinesis in higher plants. Annual Review of Plant Biology **56**, 281–299.

Jürgens G, Park M, Richter S, Touihri S, Krause C, Kasmi FE, Mayer U. 2015. Plant cytokinesis: a tale of membrane traffic and fusion. Biochemical Society Transactions **43**, 73–78.

Lebecq A, Goldy C, Fangain A, Gascon E, Belcram K, Pastuglia M, Bouchez D, Caillaud MC. 2023. The phosphoinositide signature guides the final step of plant cytokinesis. Science Advances **9**, eadf7532.

Lee YR, Liu B. 2013. The rise and fall of the phragmoplast microtubule array. Current Opinion in Plant Biology **16**, 757–763.

Lukowitz W, Mayer U, Jürgens G. 1996. Cytokinesis in the Arabidopsis embryo involves the syntaxin-related KNOLLE gene product. Cell **84**, 61–71.

Mayers JR, Hu T, Wang C, Cárdenas JJ, Tan Y, Pan J, Bednarek SY. 2017. SCD1 and SCD2 form a complex that functions with the exocyst and RabE1 in exocytosis and cytokinesis. The Plant Cell **29**, 2610–2625.

McDonald KL. 2014. Out with the old and in with the new: rapid specimen preparation procedures for electron microscopy of sectioned biological material. Protoplasma **251**, 429–448.

McDonald KL, Webb RI. 2011. Freeze substitution in 3 hours or less. Journal of Microscopy **243**, 227–233.

Miart F, Desprez T, Biot E, Morin H, Belcram K, Höfte H, Gonneau M, Vernhettes S. 2014. Spatio-temporal analysis of cellulose synthesis during cell plate formation in *Arabidopsis*. The Plant Journal **77**, 71–84.

Moore PJ, Staehelin LA. 1988. Immunogold localization of the cell-wall-matrix polysaccharides rhamnogalacturonan I and xyloglucan during cell expansion and cytokinesis in *Trifolium pratense* L.; implication for secretory pathways. Planta **174**, 433–445.

Nan Q, Liang H, Mendoza J, Liu L, Fulzele A, Wright A, Bennett EJ, Rasmussen CG, Facette MR. 2023. The OPAQUE1/DISCORDIA2 myosin XI is required for phragmoplast guidance during asymmetric cell division in maize. The Plant Cell **35**, 2678–2693.

Novák D, Vadovič P, Ovečka M, Šamajová O, Komis G, Colcombet J, Šamaj J. 2018. Gene expression pattern and protein localization of Arabidopsis phospholipase D alpha 1 revealed by advanced light-sheet and super-resolution microscopy. Frontiers in Plant Science **9**, 371.

Otegui MS. 2020. Electron tomography and immunogold labeling as tools to analyze de novo assembly of plant cell walls. Methods in Molecular Biology **2149**, 365–382.

Otegui MS, Mastronarde DN, Kang BH, Bednarek SY, Staehelin LA. 2001. Three-dimensional analysis of syncytial-type cell plates during endosperm cellularization visualized by high resolution electron tomography. The Plant Cell **13**, 2033–2051.

Ovecka M, Sojka J, Tichá M, Komis G, Basheer J, Marchetti C, Samajová O, Kubenová L, Samaj J. 2022. Imaging plant cells and organs with light-sheet and super-resolution microscopy. Plant Physiology **188**, 683–702.

Park E, Díaz-Moreno SM, Davis DJ, Wilkop TE, Bulone V, Drakakaki G. 2014. Endosidin 7 specifically arrests late cytokinesis and inhibits callose biosynthesis, revealing distinct trafficking events during cell plate maturation. Plant Physiology **165**, 1019–1034.

Park M, Mayer U, Richter S, Jürgens G. 2023. NSF/αSNAP2-mediated cis-SNARE complex disassembly precedes vesicle fusion in *Arabidopsis* cytokinesis. Nature Plants **9**, 889–897.

Parre E, Geitmann A. 2005. More than a leak sealant. The mechanical properties of callose in pollen tubes. Plant Physiology **137**, 274–286.

Piršelová B, Matušíková I. 2013. Callose: the plant cell wall polysaccharide with multiple biological functions. Acta Physiologiae Plantarum **35**, 635–644.

Qi X, Kaneda M, Chen J, Geitmann A, Zheng H. 2011. A specific role for *Arabidopsis* TRAPPII in post-Golgi trafficking that is crucial for cytokinesis and cell polarity. The Plant Journal **68**, 234–248.

Qi X, Zheng H. 2013. Rab-A1c GTPase defines a population of the trans-Golgi network that is sensitive to endosidin1 during cytokinesis in *Arabidopsis*. Molecular Plant **6**, 847–859.

Samuels AL, Giddings TH, Staehelin LA. 1995. Cytokinesis in tobacco BY-2 and root tip cells: a new model of cell plate formation in higher plants. Journal of Cell Biology **130**, 1345–1357.

Seguí-Simarro JM, Austin JR, White EA, Staehelin LA. 2004. Electron tomographic analysis of somatic cell plate formation in meristematic cells of *Arabidopsis* preserved by high-pressure freezing. The Plant Cell **16**, 836–856.

Sen O, Harrison JU, Burroughs NJ, McAinsh AD. 2021. Kinetochore life histories reveal an Aurora-B-dependent error correction mechanism in anaphase. Developmental Cell **56**, 3405.

Shi Y, Luo C, Xiang Y, Qian D. 2023. Rab GTPases, tethers, and SNAREs work together to regulate Arabidopsis cell plate formation. Frontiers in Plant Science **14**, 1120841.

Sinclair R, Hsu G, Davis D, Chang M, Rosquete M, Iwasa JH, Drakakaki G. 2022. Plant cytokinesis and the construction of new cell wall. FEBS Letters **596**, 2243–2255.

Sinclair R, Wang M, Jawaid MZ, *et al*. 2024. Data from: Four-dimensional quantitative analysis of cell plate development using lattice light sheet microscopy identifies robust transition points between growth phases. Zenodo https://doi.org/10.5281/zenodo.10515765

Smertenko A. 2018. Phragmoplast expansion: the four-stroke engine that powers plant cytokinesis. Current Opinion in Plant Biology **46**, 130–137.

Smertenko A, Assaad F, Baluška F, *et al*. 2017. Plant cytokinesis: terminology for structures and processes. Trends in Cell Biology **27**, 885–894.

Staehelin LA, Hepler PK. 1996. Cytokinesis in higher plants. Cell **84**, 821–824.

Thiele K, Wanner G, Kindzierski V, Jürgens G, Mayer U, Pachl F, Assaad FF. 2009. The timely deposition of callose is essential for cytokinesis in *Arabidopsis*. The Plant Journal **58**, 13–26.

Tichá M, Richter H, Ovečka M, Maghelli N, Hrbáčková M, Dvořák P, Šamaj J, Šamajová O. 2020. Advanced microscopy reveals complex developmental and subcellular localization patterns of ANNEXIN 1 in *Arabidopsis*. Frontiers in Plant Science **11**, 1153.

Ueda K, Sakaguchi S, Kumagai F, Hasezawa S, Quader H, Kristen U. 2003. Development and disintegration of phragmoplasts in living cultured cells of a GFP::TUA6 transgenic *Arabidopsis thaliana* plant. Protoplasma **220**, 111–118.

Ušák D, Haluška S, Pleskot R. 2023. Callose synthesis at the center point of plant development—an evolutionary insight. Plant Physiology **193**, 54–69.

van Oostende-Triplet C, Guillet D, Triplet T, Pandzic E, Wiseman PW, Geitmann A. 2017. Vesicle dynamics during plant cell cytokinesis reveals distinct developmental phases. Plant Physiology **174**, 1544–1558.

Vatén A, Dettmer J, Wu S, *et al*. 2011. Callose biosynthesis regulates symplastic trafficking during root development. Developmental Cell **21**, 1144–1155.

Vyplelová P, Ovečka M, Šamaj J. 2017. Alfalfa root growth rate correlates with progression of microtubules during mitosis and cytokinesis as revealed by environmental light-sheet microscopy. Frontiers in Plant Science **8**, 1870.

Yang J, Bak G, Burgin T, Barnes WJ, Mayes HB, Peña MJ, Urbanowicz BR, Nielsen E. 2020. Biochemical and genetic analysis identify CSLD3 as a beta-1,4-glucan synthase that functions during plant cell wall synthesis. The Plant Cell **32**, 1749–1767.

Yim KO, Bradford KJ. 1998. Callose deposition is responsible for apoplastic semipermeability of the endosperm envelope of muskmelon seeds. Plant Physiology **118**, 83–90.

Zhang L, Smertenko T, Fahy D, *et al*. 2021. Analysis of formin functions during cytokinesis using specific inhibitor SMIFH2. Plant Physiology **186**, 945–963.